Combining peridynamics and generalized interpolation material point method via volume modification for simulating transient responses

Zhixin Zeng, Yu-Chen Su, Xiong Zhang & Zhen Chen

Springer

Springer

Combining peridynamics and generalized interpolation material point method via volume modification for simulating transient responses

Zhixin Zeng[1] · **Yu-Chen Su**[2] · **Xiong Zhang**[1] · **Zhen Chen**[2,3]

Abstract

By using nonlocal discrete force functions, peridynamics (PD) can effectively deal with the problems involving discontinuities and singularities. As a continuum-based particle method, the material point method (MPM) and its advanced version, generalized interpolation material point method (GIMP), use local and nonlocal spatial discretization, respectively, to effectively simulate large deformations and multi-phase (solid–fluid–gas) interactions via mapping and remapping between material points and associated background nodes. However, nonlocal constitutive modeling has rarely been employed in the MPM or GIMP for simulating failure evolution. To combine the strengths of both PD and MPM/GIMP for better simulating the failure evolution under transient loading, an attempt is made to eliminate the limitation in the original PD due to the volume integration so that both MPM/GIMP and PD could be smoothly combined via volume modification. One-dimensional examples are employed to demonstrate and verify the proposed volume modification peridynamics and its combination with MPM/GIMP.

Keywords Volume modification peridynamics · MPM · GIMP · Impact failure

1 Introduction

There has been an increasing interest in peridynamics (PD) that evolved based on a nonlocal theory [1, 2] of continuum mechanics in the past decades. PD replaces the spatial derivatives of the classical continuum mechanics with the integral equations. Due to this nonlocal feature, PD has been widely adopted as an effective numerical approach to deal with the discontinuities and singularities in solids [3, 4], such as dynamic crack growth and fatigue crack growth.

Based on the description of the forcing function, PD can be divided into two different frameworks, namely bond based and state based [5–13]. In the bond-based PD, only the central forces between two particles are considered. These central forces are obtained with the use of the spatial derivatives of the inter-particle potential energy that is a function of their corresponding relative displacements. Therefore, the bond-based forces between the two particles are opposite in direction and equal in magnitude, and they also automatically satisfy the conservation of linear and angular momentum, respectively. The bond-based PD has been commonly used due to its simplicity. However, there is a limitation in the bond-based PD, namely, the Poisson's ratio is restricted to 1/4in 3-D and 2-D plane strain cases [14], and restricted to 1/3 in the 2-D plane stress case [14]. In the state-based PD, there are two different formulations that are ordinary and non-ordinary [6, 10–13]. The main difference between these two types of state-based PD is the description of the force state. Similar to the bond-based PD, only the couple of opposite central forces between any two particles are considered in the ordinary state-based PD. However, the couple of the opposite central forces may not be equal in magnitude such that the conservation of linear momentum cannot be satisfied. On the other hand, the central forces of the ordinary state-based PD are still aligned to satisfy the conservation of angular momentum. Different from the bond-based PD and ordinary state-based PD, the inter-particle forces in the non-ordinary state-based PD are neither opposite in direction nor equal in magnitude. The state-based PD approach has been widely adopted to predict the material behaviors including elasticity

✉ Zhen Chen
chenzh@missouri.edu

1   School of Aerospace Engineering, Tsinghua University, Beijing 100084, People's Republic of China

2   Department of Civil and Environment Engineering, University of Missouri, Columbia, MO 65211, USA

3   State Key Laboratory of Structural Analysis for Industrial Equipment, Department of Engineering Mechanics, Faculty of Vehicle Engineering and Mechanics, Dalian University of Technology, Dalian 116024, People's Republic of China

[14, 15], plasticity [16], and fracture [17]. For the purpose of simplicity, however, the bond-based PD will be considered here for one-dimensional verification and demonstration.

With its unique capability in fracture mechanics, PD has been combined with other continuum-based numerical approaches such as the finite element method (FEM) [18, 19]. However, there are some limitations in the combined PD/FEM procedure. First, a complicated interfacial treatment is required to be implemented between the PD regions and FEM regions. Second, FEM is not a suitable method for large deformation problems because the need for re-meshing [20–22]. Therefore, an attempt is made in this work to combine PD with the material point method (MPM) that has been developed for large deformation and multi-phase interaction problems [23, 24]. Because both the PD and MPM belong to the particle methods, the interfacial treatment for the PD/MPM model would be simpler than that for the PD/FEM model. For better dealing with the large deformation cases, a generalized interpolation material point method (GIMP) [25, 26] was proposed by replacing the local mapping and remapping operation within a single cell in the MPM with a nonlocal one over several cells such that the cell crossing issue could be eliminated at an additional computational cost. Hence, the numerical procedure for combined PD and GIMP will be designed, in which combining PD and MPM is a special case.

The remaining sections of this paper are organized as below. The basic formulations of MPM and GIMP are summarized in Sect. 2. The introduction of the bond-based PD is given in Sect. 3, in which a volume modification PD (VMPD) is proposed to eliminate the integration error. The combination procedures for both PD/MPM and PD/GIMP are described in Sect. 4. In Sect. 5, a 1-D bar is used for demonstration and verification. First, the comparison of the elastic stress wave propagation as obtained with the MPM, GIMP, PD, and VMPD, respectively, is shown for transient tensile loading. Second, the similar 1-D simulations with the use of an elastoplasticity model are performed. Finally, a combination of elasticity and fracture mechanics is implemented into the 1-D bar model subject to an impact load to illustrate the respective strengths of PD and GIMP.

2 MPM and GIMP

2.1 MPM

In the MPM, a continuum body is discretized into a finite set of N_p Lagrangian material points (particles) carrying all the state variables. Therefore, the mass density and the weak form of the conservation of linear momentum can be expressed as follows:

$$\rho(\boldsymbol{x}, t) = \sum_{p=1}^{N_p} M_p \delta\left(\boldsymbol{x} - \boldsymbol{x}_p^t\right), \tag{1}$$

$$\int_\Omega \rho \boldsymbol{w} \cdot \boldsymbol{a} \mathrm{d}\Omega + \int_\Omega \rho \boldsymbol{\sigma}^s : \nabla \boldsymbol{w} \mathrm{d}\Omega - \int_\Omega \rho \boldsymbol{w} \cdot \boldsymbol{b} \mathrm{d}\Omega$$
$$- \int_{\Gamma_\sigma} \rho \bar{\boldsymbol{\tau}}^s \cdot \boldsymbol{w} \mathrm{d}\Gamma = 0. \tag{2}$$

In Eq. (1), $\boldsymbol{x}$ and M_p represent the position vector and the mass of material point p, and δ is the Dirac delta function. In Eq. (2), $\boldsymbol{a}$ is the acceleration, $\boldsymbol{b}$ is the specific body force, $\boldsymbol{w}$ is the test function, $\boldsymbol{\sigma}^s = \boldsymbol{\sigma}/\rho$ is the specific stress, $\bar{\boldsymbol{\tau}}^s = \bar{\boldsymbol{\tau}}/\rho$ is the specific traction on the boundary Γ_σ, and Ω is the problem domain of the continuum body. Substituting Eq. (1) for the mass density ρ into Eq. (2) results in

$$\sum_{p=1}^{N_p} M_p \left[\boldsymbol{w}\left(\boldsymbol{x}_p^t\right) \cdot \boldsymbol{a}\left(\boldsymbol{x}_p^t\right) \right]$$
$$= \sum_{p=1}^{N_p} M_p \left\{ -\boldsymbol{\sigma}_p^s\left(\boldsymbol{x}_p^t\right) : \nabla \boldsymbol{w}|_{\boldsymbol{x}_p^t} + \boldsymbol{w}\left(\boldsymbol{x}_p^t\right) \cdot \boldsymbol{b}\left(\boldsymbol{x}_p^t\right) \right\}$$
$$+ \int_{\Gamma_\sigma} \rho \boldsymbol{w}\left(\boldsymbol{x}_p^t\right) \cdot \bar{\boldsymbol{\tau}}^s \mathrm{d}\Gamma \tag{3}$$

By using the nodal basis functions, the discretized governing equation for the material point, as expressed in Eq. (3), can be rewritten as that with respect to their corresponding background grid nodes I, that is

$$m_I^t \boldsymbol{a}_I^t = (\boldsymbol{f}_I^t)^{\mathrm{int}} + (\boldsymbol{f}_I^t)^{\mathrm{ext}}, \tag{4}$$

in which, m_I^t is the lumped nodal mass, $(\boldsymbol{f}_I^t)^{\mathrm{int}}$ and $(\boldsymbol{f}_I^t)^{\mathrm{ext}}$ are the internal and external load of the grid node I, as given as follows:

$$m_I^t = \sum_{p=1}^{N_p} M_p N_I\left(\boldsymbol{x}_p^t\right), \tag{5}$$

$$(\boldsymbol{f}_I^t)^{\mathrm{int}} = -\sum_{p=1}^{N_p} \frac{M_p}{\rho_p^t} \boldsymbol{\sigma}_p^t \nabla N_I\left(\boldsymbol{x}_p^t\right), \tag{6}$$

$$(\boldsymbol{f}_I^t)^{\mathrm{ext}} = \sum_{p=1}^{N_p} M_p N_I\left(\boldsymbol{x}_p^t\right) \boldsymbol{b}\left(\boldsymbol{x}_p^t\right) + \int_{\Gamma_\sigma} N_I\left(\boldsymbol{x}_p^t\right) \bar{\boldsymbol{\tau}} d\Gamma. \tag{7}$$

In Eqs. (5)–(7), $N_I\left(\boldsymbol{x}_p^t\right)$ and $\nabla N_I\left(\boldsymbol{x}_p^t\right)$ are the nodal basis function (or mapping function between material points and their corresponding grid nodes in the MPM) and its corresponding gradient associated with node I evaluated at the

material point position vector x_p^t. The nodal basis function $N_I(x)$ in 1-D domain takes the form of

$$N_I(x) = \begin{cases} 0, & x - x_I \leq -L \\ 1 + (x - x_I)/L, & -L < x - x_I \leq 0 \\ 1 - (x - x_I)/L, & 0 < x - x_I \leq L \\ 0, & L < x - x_I \end{cases}, \quad (8)$$

where x_I is the position vector of background grid node I, and L is the background grid cell length. Since the nodal basis function defined within a single cell is zero outside the given cell, it represents the local mapping and remapping operation for a particle within the given cell no matter how the particle deforms. As a result, the cell-crossing error might occur as a material point crosses the cell boundary.

2.2 GIMP

In the GIMP, the discretized governing equations are the same as those in the MPM, but the mapping and remapping operations become nonlocal over several cells. In order to avoid the cell crossing issue in the MPM, the local basis function, $N_I\left(x_p^t\right)$, is replaced by a nonlocal one, $\bar{N}_I\left(x_p^t\right)$, as expressed in Eq. (9). Hence, the main difference between the MPM and GIMP is that the nodal basis function, $\bar{N}_I\left(x_p^t\right)$, covers not only the given grid cell but also its neighboring cells due to the particle deformation, namely

$$\bar{N}_I(x_p^t) = \begin{cases} 0, & \left|x_p^t - x_I\right| \geq L + l_p \\ \frac{(L + l_p + x_p^t - x_I)^2}{4Ll_p}, & -L - l_p < x_p^t - x_I \leq -L + l_p \\ 1 + \frac{x_p^t - x_I}{L}, & -L + l_p < x_p^t - x_I \leq -l_p \\ 1 - \frac{(x_p^t - x_I)^2 + l_p^2}{2Ll_p}, & -l_p < x_p^t - x_I \leq l_p \\ 1 - \frac{x_p^t - x_I}{L}, & l_p < x_p^t - x_I \leq L - l_p \\ \frac{(L + l_p - x_p^t + x_I)^2}{4Ll_p}, & L - l_p < x_p^t - x_I \leq L + l_p \end{cases}$$

(9)

where $2l_p$ represents the particle size and other variables are the same as those in Eq. (8). The detailed discussion about the difference between the MPM and GIMP is given in Ref. [25].

3 Peridynamics

3.1 Discrete governing equation of PD

In PD, a nonlocal extension of continuum mechanics, namely, a material point x interacts directly with all the adjacent material points x' within a finite distance δ (cutoff radius). For any

$x \in B$, $B = \{x' | \|x' - x\| < \delta\}$, the equation of motion for PD can be written as

$$\rho(x)\ddot{u}(x,t) = \int_B f(x,x',u,u')dV_{x'} + b(x,t), t \geq 0,$$

(10)

where $u(x,t)$ and $u'(x,t)$ are the displacement fields for particle x and x', $b(x,t)$ is the loading force density, and $\rho(x)$ is the mass density. Additionally, the vector function $f(x,x',u,u')$ is the force density (force per unit volume) per unit reference volume exerted on a particle $y = x + u$ (x,t) by another particle $y' = x' + u'(x,t)$. Furthermore, the forcing function is determined by the gradient of a pairwise micropotential function $w(x,x',u,u')$, and the relationship between the pairwise micropotential function and the forcing function is expressed as follows:

$$f(x,x',u,u') = \nabla_{u-u'} w(x,x',u,u').$$

(11)

Integrating the equation of motion for PD in a configuration Ω results in

$$\int_\Omega \rho(x)\ddot{u}(x,t)\,dV_x = \int_\Omega \int_{B/\Omega} f(x,x',u,u')\,dV_{x'}dV_x \\ + \int_\Omega b(x,t)\,dV_x.$$

(12)

Equation (12) is rewritten in a discretized form,

$$m_x\ddot{u}(x,t) = \sum_{x'\in B}\left(f(x,x',u,u')V_{x'}V_x\right) + b(x,t)V_x \quad (13)$$

where $m_x = \rho(x)V_x$.

3.2 Isotropic elastic PD

Since the forcing function considered here employs the bond-based PD approach, the harmonic oscillation potential energy is suitable for describing the inter-particle potential energy. Therefore, the micropotential per unit volume squared and force per unit volume squared are given by

$$w(x,x',u,u') = \frac{k}{2}\frac{(\|x' + u' - x - u\| - \|x' - x\|)^2}{\|x' - x\|},$$

(14)

$$f(x,x',u,u') \\ = k\frac{\|x' + u' - x - u\| - \|x' - x\|}{\|x' - x\|}\frac{x' + u' - x - u}{\|x' + u' - x - u\|},$$

(15)

where $k/\|x' - x\|$ is the stiffness per unit volume squared [5, 27]. Additionally, $\|x' - x\|$ is the equilibrium distance between particles x and x'

3.3 Isotropic elastoplastic PD

An elastoplastic model is used here to investigate the elastoplastic behaviors by using PD [28–30]. Similar to the general elastoplastic deformation theory, the bond strain between two PD particles, i and j, can be decomposed into two components, elastic and plastic components, as follows:

$$s_{ij}^d = s_{ij}^e + s_{ij}^p, \tag{16}$$

$$s_{ij}^d = \frac{\|x_j + u_j - x_i - u_i\| - \|x_j - x_i\|}{\|x_j - x_i\|}, \tag{17}$$

where s_{ij}^e and s_{ij}^p are the elastic and plastic components of the total bond strain, s_{ij}^d, respectively. As a result, the corresponding force density per unit volume squared can be written as

$$f\left(x, x', u, u'\right) = \left\{k^e s_{ij}^e + k^p s_{ij}^p\right\} \frac{x' + u' - x - u}{\|x' + u' - x - u\|}, \tag{18}$$

in which, k^e and k^p are the force constant per unit volume squared for elastic and plastic deformations, respectively. Taking a one-dimensional PD bar for example, $k^e = \frac{2E^e}{A\delta^2}$ and $k^p = \frac{2E^p}{A\delta^2}$, where A is the cross-sectional area, E^e and E^p are the Young's modulus and plastic tangential modulus, and δ is the cutoff radius, respectively [31, 32].

3.4 Fracture model of PD

In addition to the elastic and elastoplastic models, a fracture model [27, 33] is also adopted here to demonstrate the fracture (or discontinuity) feature. In the fracture model with PD, a critical bond strain s_{cri} and a history-dependent scalar function θ are required, and their relationship is given by

$$\theta = \begin{cases} 1, & s_{\max} < s_{\text{cri}} \\ 0, & s_{\max} > s_{\text{cri}} \end{cases}, \tag{19}$$

where $s_{\max} = (\|x' + u' - x - u\| - \|x' - x\|)/\|x' - x\|$ is the maximum bond strain between two PD particles. Furthermore, the history-dependent scalar function θ is used to multiply with the inter-particle force density per unit volume squared, $f\left(x, x', u, u'\right)$, namely

$$\begin{aligned} f\left(x, x', u, u'\right) \\ = \theta k \frac{\|x' + u' - x - u\| - \|x' - x\|}{\|x' - x\|} \frac{x' + u' - x - u}{\|x' + u' - x - u\|}, \end{aligned} \tag{20}$$

which means that the inter-particle force will be zero when the bond strain is larger than the user-defined critical strain.

3.5 Volume modification PD

The cutoff radius plays an important role in the integration process in PD. However, the original definition of the cutoff radius would lead to some numerical errors. Figure 1 shows a PD model with two different cutoff radii, δ. In original PD integration definition, although the cutoff radii for these two models are different, the required particles for calculating the internal force of particle 3 are the same, which are particles 2 and 4. It is because the mass centers of particles 2 and 4 are within the cutoff radius, while those of particles 1 and 5 are not. In the model of Fig. 1b, however, a numerical error exists because the cutoff radius has covered the volume boundary of particles 1 and 5. In order to eliminate this numerical error, the cutoff radius is modified from δ to $\delta + l_e/2$. As shown in Fig. 1, the variable l_e is the length covered by one PD particle. With this modified definition, thus, particles 1 and 5 are still not counted in model 1(a), but these two particles are counted in model 1(b). This modification method is called volume modification of PD (VMPD).

4 Combination algorithm

4.1 Combination algorithm with unified background grids

Preprocessor:

1. Discretize a continuum body into PD particles and MPM particles in the respective region, as shown in Fig. 2a. Each particle carries the required properties such as mass and material properties.
2. Define unified background grids, and identify the grid cells in which specific PD and MPM particles are located.
3. Implement the boundary and initial data, as well as the control parameters for the simulation.

Central Processor in Each Time Step:

1. Map the variables including the mass, momentum, and internal force from all the PD and MPM particles to their corresponding background grid nodes as follows:

$$m_I^t = \sum_{p=1}^{N_P} M_P N_I\left(x_p^t\right), \tag{21}$$

$$(mv)_I^t = \sum_{p=1}^{N_P} (Mv)_p^t N_I\left(x_p^t\right), \tag{22}$$

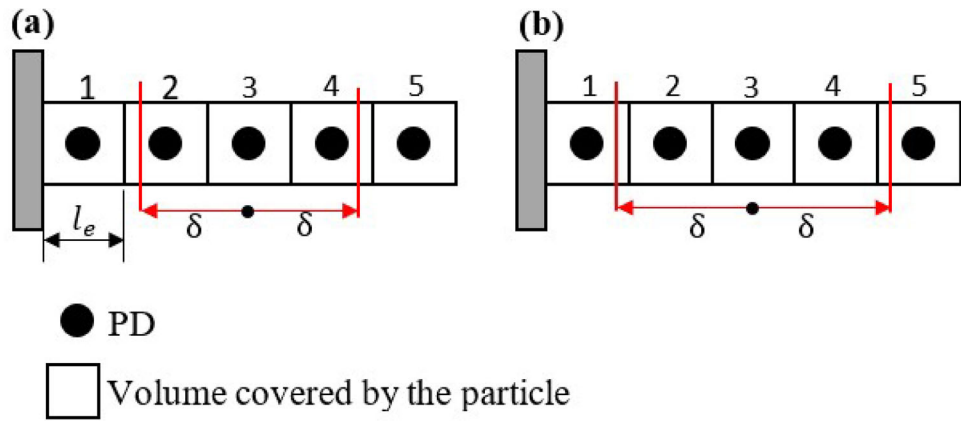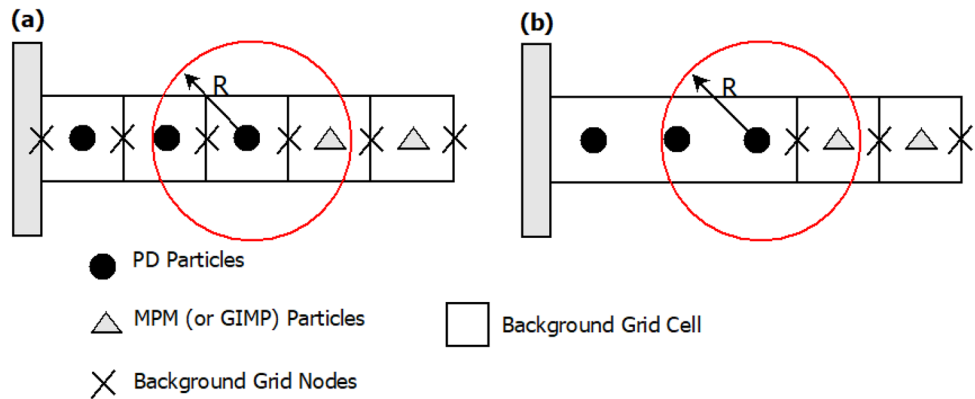**Fig. 1** The PD models with different cut-off radii

Fig. 2 a PD/MPM (or PD/GIMP) model with a unified background grid. **b** PD/MPM (or PD/GIMP) model without a unified background grid

$$(f_I^t)^{int} = \sum_{p=1}^{N_{p1}} f_p^t N_I\left(x_p^t\right) - \sum_{p=N_{p1}+1}^{N_{p1}+N_{p2}} \sigma_p^t \frac{m_p}{\rho_p^t} \nabla N_I\left(x_p^t\right), \tag{23}$$

where m_I^t is the mass at node I at time t, M_P is the mass of particle p, N_I is the mapping function associated with node I, x_p^t is the position vector of the particle p at time t, $(mv)_I^t$ is the nodal momentum at node I and time t, $(Mv)_p^t$ is the particle momentum at the same time step, f_p^t is the internal force of PD particles (MPM particle within the PD cutoff radius may also have this part), σ_p^t is the stress tensor of the MPM particles, and N_{p1}, N_{p2} are, respectively, the total number of PD and MPM particles that are located in the same background cell [34].

2. Apply the essential and natural boundary conditions to the grid nodes and compute the nodal forces,

$$f_I^t = (f_I^t)^{int} + (f_I^t)^{ext}, \tag{24}$$

in which $(f_I^t)^{ext}$ represents the external force at node I.

3. Integrate the momentum at each node,

$$(mv)_I^{t+\Delta t} = (mv)_I^t + f_I^t \Delta t, \tag{25}$$

where Δt is the integration time step.

4. Update the velocity vector and position vector of each PD and MPM particle for the time step $t + \Delta t$ via the remapping process from the background grid node to its associated particles.

$$v_p^{t+\Delta t} = v_p^t + \Delta t \sum_{I=1}^{N_n} \frac{f_I^t}{m_I^t} N_I\left(x_p^t\right), \tag{26}$$

$$x_p^{t+\Delta t} = x_p^t + \Delta t \sum_{I=1}^{N_n} \frac{(mv)_I^{t+\Delta t}}{m_I^t} N_I\left(x_p^t\right). \tag{27}$$

With the above information, update the inter-particle force vector of each PD particle, $f_p^{t+\Delta t}$, by using the PD micropotential function. For calculating the force vector of a specific PD particle, the adjacent MPM particles must be counted in the calculating process if they are within the corresponding PD cut-off radius.

5. Map the updated momentum of each MPM or PD particle back to its corresponding background nodes to evaluate the updated nodal velocity, namely

$$(mv)_I^{t+\Delta t} = \sum_{p=1}^{N_P} (Mv)_p^{t+\Delta t} N_I\left(x_p^t\right), \tag{28}$$

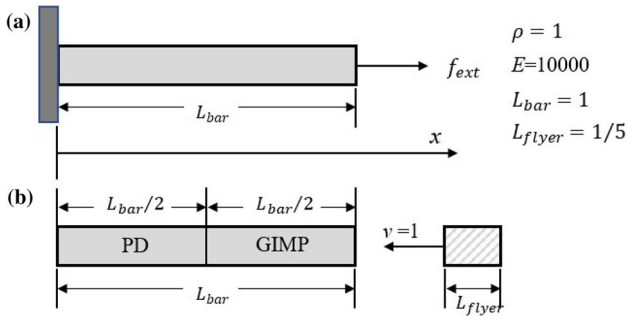$$v_I^{t+\Delta t} = \frac{(mv)_I^{t+\Delta t}}{m_I^t}. \tag{29}$$

Fig. 3 A 1-D bar with two different types of load

6. Find the current gradient of the velocity vector for each MPM particle,

$$L_p^{t+\Delta t} = \sum_{I=1}^{N_n} v_I^{t+\Delta t} \nabla N_I\left(x_p^t\right). \tag{30}$$

Then, calculate the strain increment of each MPM particle,

$$\Delta\varepsilon_p^t = \frac{1}{2}\left(L_p^{t+\Delta t} + \left(L_p^{t+\Delta t}\right)^T\right)\Delta t. \tag{31}$$

7. Update the current stress tensor of each MPM particle via the constitutive model and Eq. (31),

$$\sigma_p^{t+\Delta t} = \sigma_p^t + D : \Delta\varepsilon_p^t \tag{32}$$

where D is the tangent stiffness tensor obtained from the material model.

8. Go back to Step 1 in the central processor until the terminal time is reached for output.

If the MPM part in the above algorithm is replaced by the GIMP, the mapping and remapping function $N_I\left(x_p^t\right)$ will be changed to $\bar{N}_I\left(x_p^t\right)$, as expressed in Eq. (9).

4.2 Combination algorithm without unified background grids

In order to investigate whether the background grid nodes would affect the simulation accuracy, another combination algorithm without the unified background grid nodes is also designed. As shown in Fig. 2b, the MPM or GIMP particles are still located within a set of background grid cells, but these cells do not cover the PD particles. Therefore, all the variables associated with the PD particles are not required to be mapped to the background grid nodes unless they are within the interfacial cell adjacent to the MPM particles. In the interfacial cell, the variables associated with the PD particles will be mapped to and remapped from the grid node

shared by the adjacent MPM particles. In other words, the grid node shared by both MPM and PD particles will feel the force calculated by the MPM constitutive model and the PD discrete forcing function, respectively. If an MPM particle is within the cut-off radius of a PD particle, the MPM particle will be treated as a PD particle with the corresponding forcing function, which is similar to the concurrent multiscale procedure that involves both molecular dynamics and MPM [34].

5 Numerical demonstration

In this section, a 1-D bar with two different types of load, as shown in Fig. 3, are used to compare the simulation results with different numerical approaches. These two types of load include a unit tensile force and an impact load, respectively. For the model in Fig. 3a, the results with the use of MPM, GIMP, PD, and VMPD are compared in Sect. 5.1. With the same model, the combination solution algorithms detailed in Sect. 4 are demonstrated in Sect. 5.2. In Sect. 5.3, the constitutive model of this bar is changed from the elastic one to elastoplastic one to verify the nonlinear behaviors as obtained with the proposed procedure. Finally, the fixed boundary condition in Fig. 3a for the bar model is replaced by the free boundary condition, and a flyer with a given velocity is used to mimic the impact loading type, as shown in Fig. 3b. Additionally, the fracture model is implemented in the target to investigate the fracture behavior via the combination solution algorithm.

5.1 Comparison of MPM, GIMP, PD, and VMPD results for elastic responses

Figure 3a shows an elastic bar, which is fixed at left end and subjected to a unit tensile step force at the right end. The related material and geometrical properties are also shown in Fig. 3. In order to study the difference between each simulation method, this tensile simulation is conducted by using MPM, GIMP, PD, and VMPD, respectively.

For all the simulation methods, the total number of the particles, N_p, and time step, Δt, are set as 200 and 5×10^{-6} s, respectively. For MPM and GIMP models, this 1-D bar is within 200 grid cells. It means that each cell has one MPM or GIMP particle. For PD and VMPD models, the cut-off radius, δ, is set as $3l_e$, where l_e is defined in Sect. 3.5. The stress wave propagation along the bar at different time steps with different models are shown in Fig. 4. It can be seen that the results with PD model show the lower stress value and higher wave velocity than those with other three models. However, the results with VMPD are consistent with those via MPM and GIMP models. The difference between PD
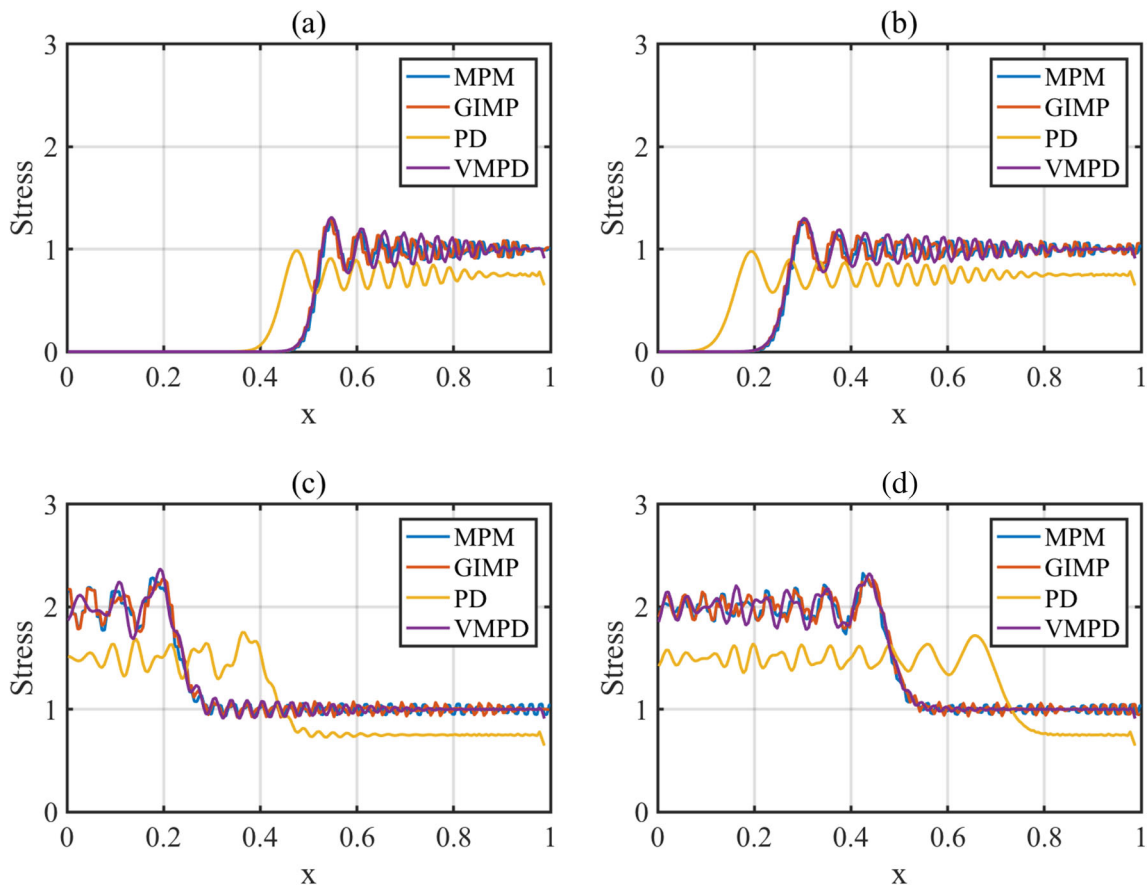
Fig. 4 The stress wave profiles along the bar at different time steps: **a** $t = 0.5L_{bar}/C$, **b** $t = 0.75L_{bar}/C$, **c** $t = 1.25L_{bar}/C$, **d** $t = 1.5L_{bar}/C$, with $C = \sqrt{E/\rho}$ being the sound speed of the bar
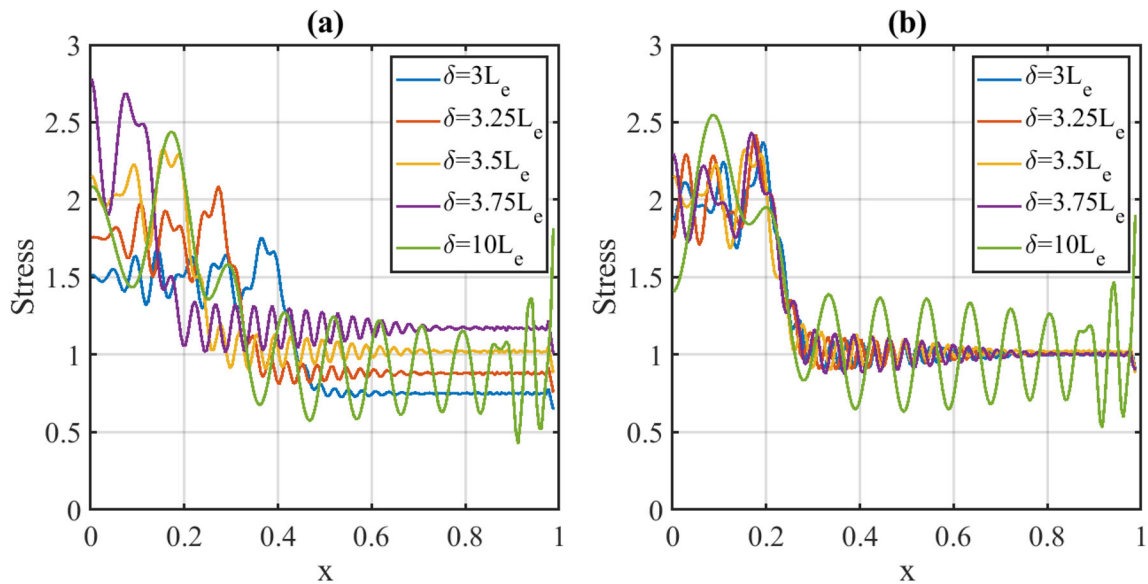

Fig. 5 The stress wave profiles along the bar at $t = 1.25L_{bar}/C$ by using **a** PD and **b** VMPD with different cut-off radii, with $C = \sqrt{E/\rho}$ being the sound speed of the bar

and VMPD is mainly caused by the integration domain (or integration volume) issue as discussed in Sect. 3.5.

In order to further demonstrate the influence of the integration volume on the PD and VMPD algorithms, several

results with different cut-off radii by using the PD and VMPD algorithms are compared in Fig. 5. It can be found that the cut-off radius largely affects the simulation accuracy with the PD algorithm. However, this issue is not obvious with the VMPD algorithm. Except for the case with the largest cut-off radius, $\delta = 10l_e$, the stress wave propagation curves with the other cut-off radii in the VMPD algorithm are close to each other. It means that the varied cutoff radius could not affect the simulation accuracy in the proposed VMPD algorithm if the cutoff radius is within a suitable range. In other words, the volume modification in the VMPD algorithm plays an important role in enhancing the accuracy of the PD algorithm.

5.2 Comparison of the combination algorithms

The 1-D bar model in Sect. 5.1 is also used to verify the combination algorithms. The right half part of the bar, which is between 0.5 and 1 in the longitudinal axis, consists of 100 MPM or GIMP particles. Similarly, the left half part

of the bar, between 0 and 0.5, includes 100 VMPD particles. In addition to the geometrical setting, the cutoff radius for the PD particle is $3\ l_e$, and the related material properties and integration time step are the same as those in Sect. 5.1. In order to investigate whether the background grid would affect the simulation results, this simulations with the combination algorithm are, respectively, performed with and without the unified background grid. Therefore, there are totally four different simulations that are PM, PG, PMG, and PGG, respectively. The PM and PG represent that the simulations combine VMPD and MPM (or GIMP) particles without the unified background grid, as shown in Fig. 2b. It means that all the variables of MPM or GIMP particles are required to be mapped to the background grids but those of VMPD particles are not. For the simulations with the PMG and PGG, the last character, G, denotes that the unified background grids cover all the VMPD and MPM (or GIMP) particles, as shown in Fig. 2a.

Figure 6 shows the stress wave propagations along the bar at different time steps associated with different algorithms.
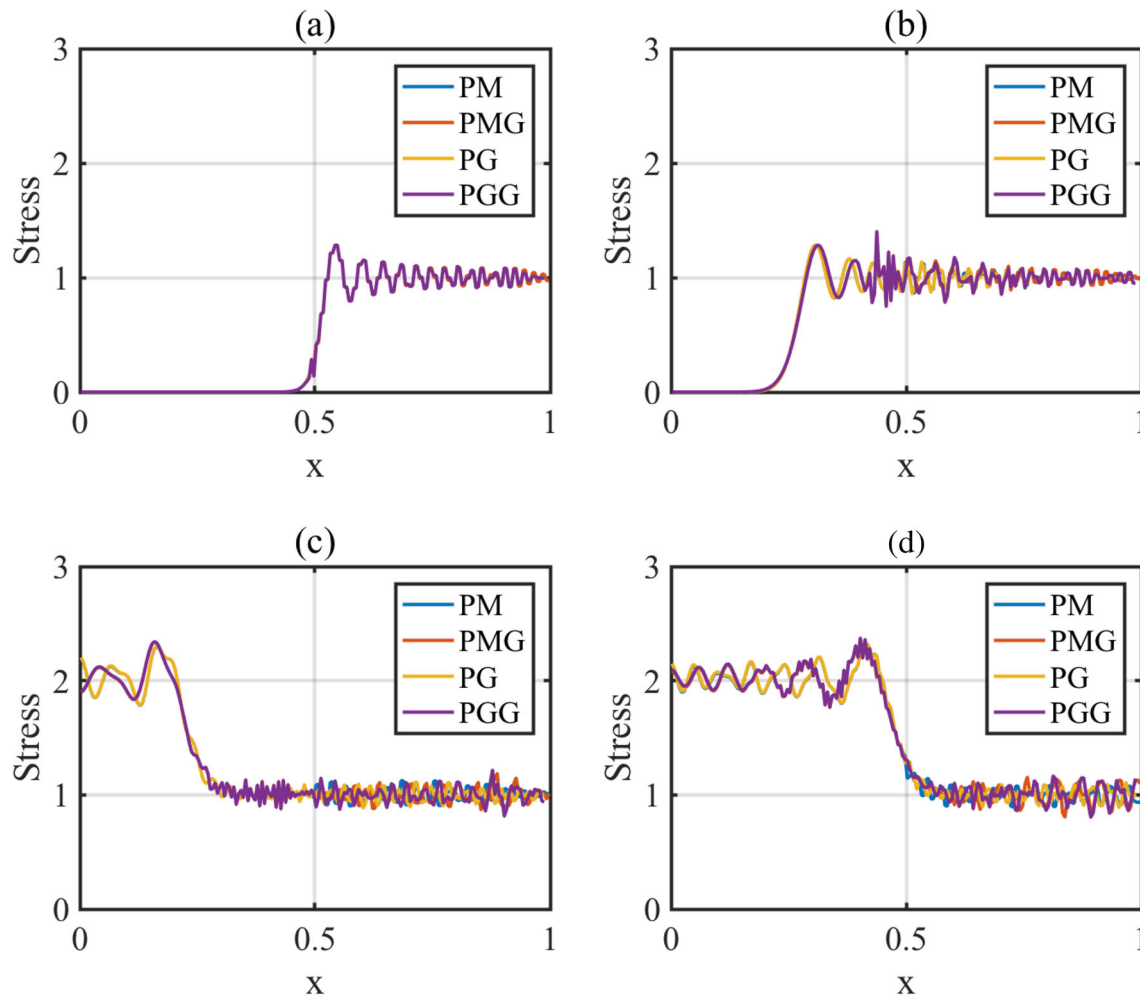

Fig. 6 The stress wave profiles along the bar by using different combination solution schemes at different time steps: **a** $t = 0.5L_{bar}/C$, **b** $t = 0.75L_{bar}/C$, **c** $t = 1.25L_{bar}/C$, and **d** $t = 1.5L_{bar}/C$
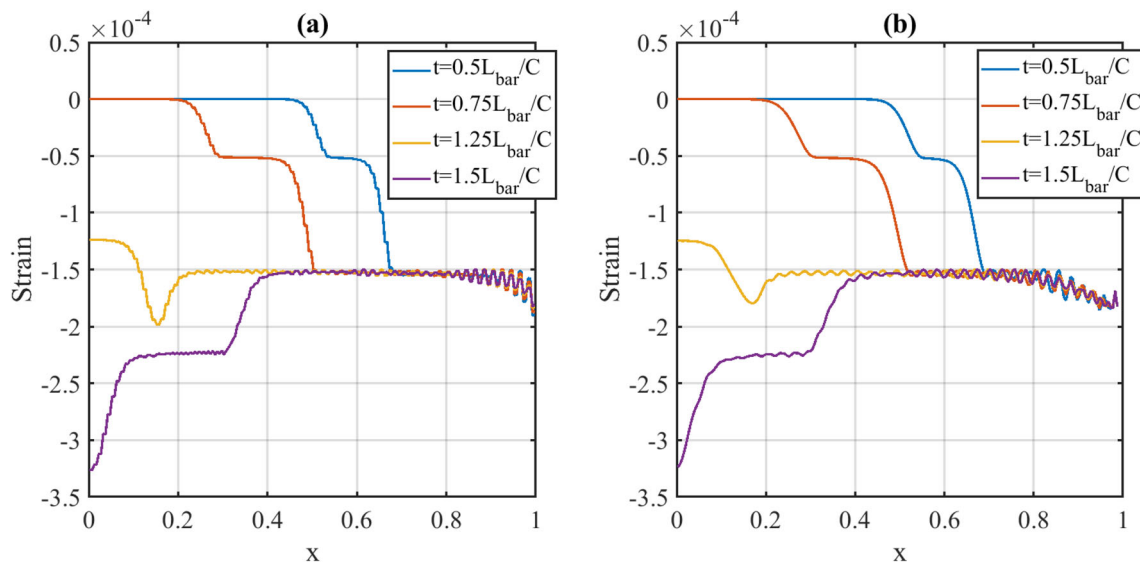
Fig. 7 The strain distribution along the bar at different time steps via **a** MPM and **b** VMPD
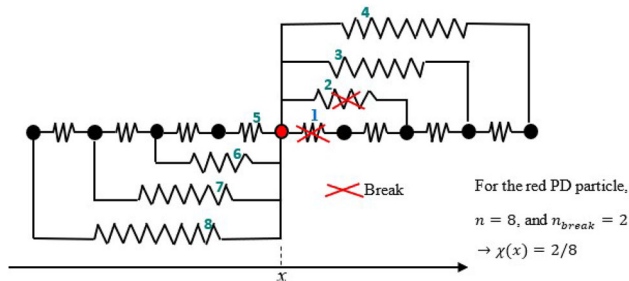

Fig. 8 The model for the PD bonds

It can be noted that there is no huge difference between the results with these four algorithms. Taking a further look at these four simulation results, however, those with the PMG and PGG show an oscillation feature (or numerical noises) near the interface, $x = 0.5$. Hence, the background grids in the VMPD domain would lead to some numerical noises.

5.3 Demonstration with an elastoplastic model

In this section, the load in Fig. 3a is changed from the tensile load to compressive load, and an elastoplastic model is implemented in the PD algorithm to verify the accuracy of the nonlinear PD simulation. For the elastoplastic model, the yield strain and hardening modulus were set as 5×10^{-5} and 5000, respectively. The simulation with this elastoplastic model and MPM algorithm is conducted as a reference for comparison. The strain distribution along the bar at different time steps with the PD and MPM are shown in Fig. 7. It can be observed that the results by using PD are in line with those by using MPM. In other words, PD can effectively predict the nonlinear mechanical behaviors of the material.

5.4 Illustration with a fracture model under impact

To take advantage of the MPM strength in simulating impact and the PD strength in simulating fracture, a fracture model is used here to predict the impact response, in which the critical bond strain in Eq. (19), s_{cri}, and the cut-off radius are set as 7.9×10^{-3} and $3\,l_e$, respectively. As shown in Fig. 3b, a 1-D bar target is impacted by a flyer, and the bar target includes a left half part of PD particles and a right half part of GIMP particles without a unified background grid. The number of the PD and GIMP particles are both 100. The PG algorithm in Sect. 5.2 is utilized to solve this combination problem. Here, a broken parameter, $\chi_{break}(x) = \frac{n_{break}}{n}$, is defined as the damage condition of the bar target, where n_{break} is the number of the broken bonds for particle x and n is the total number of the bonds associated with particle x. In other words, n_{break} represents the number of bonds that are connected to particle x with zero of the scalar-valued function (θ) in Eq. (19). For instance, as shown in Fig. 8, there are eight connection bonds for the red PD particle with position x, and two of them are broken (their bond strains are larger than 7.9×10^{-3}). Therefore, the broken number at position of x, $\chi_{break}(x)$, should become 2/8. The stress wave distribution and broken parameter $\chi_{break}(x)$ along the bar at different time steps are shown in Figs. 9 and 10, respectively. When the flyer impacts the bar target, the time is set as zero. At $t = 0.9L_{bar}/C$, the compressive stress wavefront would reach the position $x = 0.1$, and the length of wave impulse is about $0.4L_{bar}$, which is roughly from 0.1 to $0.5\ L_{bar}$. At $t = 1.2L_{bar}/C$, the stress is about zero along the whole bar target because the compressive and tensile stress waves are canceled with each other. The tensile stress wave then starts to occur near $x = 0.2$ after the time of $1.2L_{bar}/C$. As demonstrated in Fig. 9c, hence, the
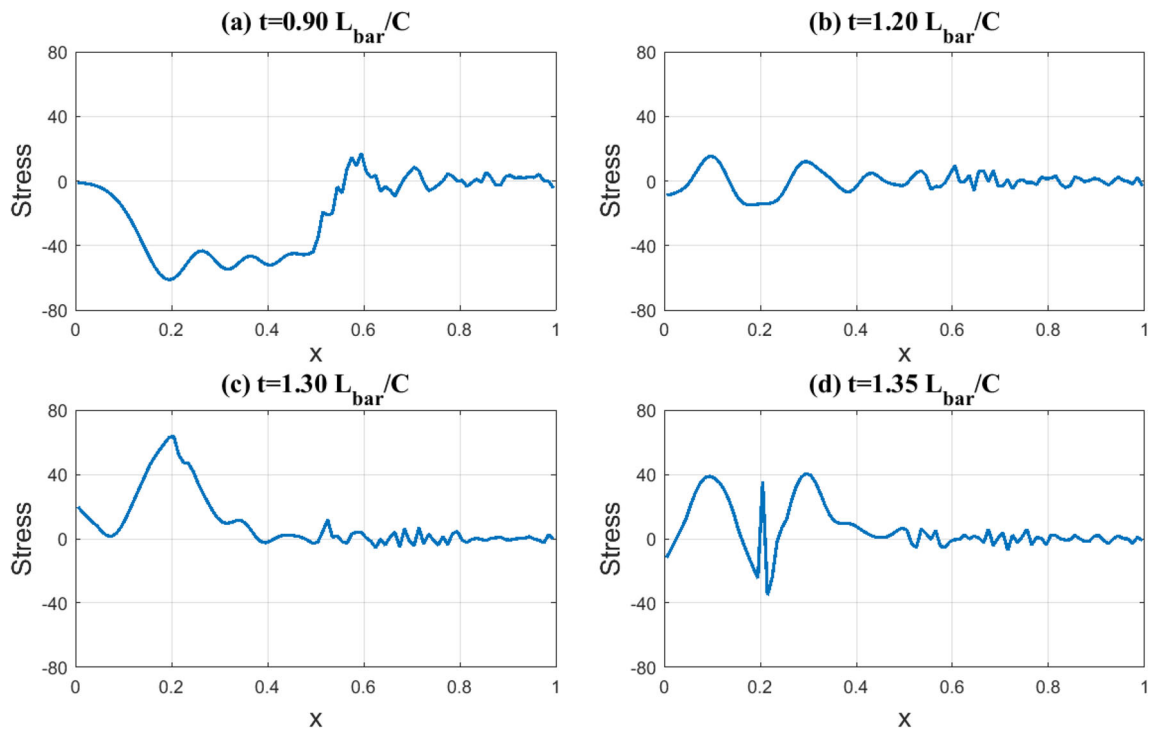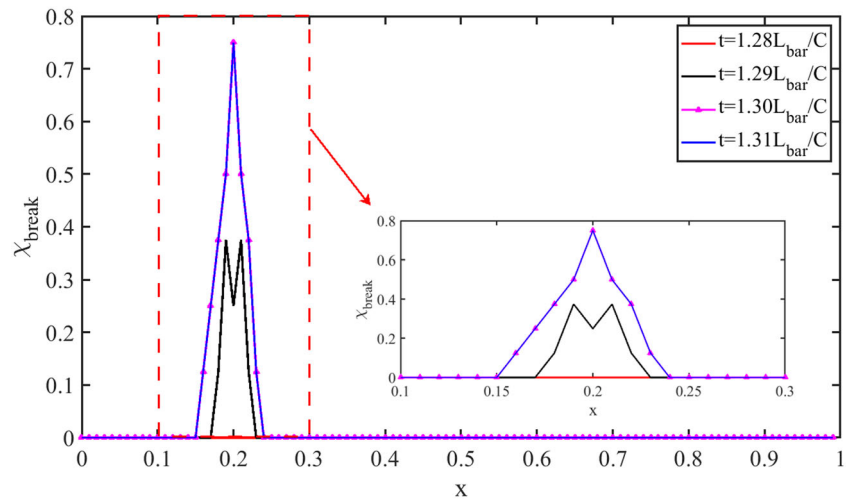
Fig. 9 The stress profiles along the bar target at different time steps

Fig. 10 The distribution of the broken parameter, $\chi(x)$, at different time steps

tensile failure might occur at $x = 0.2$, which could break the PD particle bonds. The fracture behavior is also displayed in Fig. 10, in which the initial broken bonds occur near $x = 0.2$. When $t > 1.28 L_{bar}/C$, the tensile stress becomes large enough to break the bonds.

6 Concluding remarks

An attempt has been made to combine MPM with PD in a single computational domain in which the nonlocal forcing function in PD could be combined with the local constitu-

tive model in MPM to simulate the evolution of failure under transient loadings. One-dimensional verification and demonstration have been performed with reasonable outcomes. The major findings from this work are summarized as follows:

1. A numerical error inherent in the PD algorithm is identified, and a volume modification PD could be employed to reduce the integration error.
2. The simulation results with both combination schemes including PM, PG, PMG, and PGG are consistent. However, a minor oscillation of the stress wave profile occurs near the interface between the PD and MPM (or GIMP)

regions if the unified background grids cover all the simulation domain.

3. In the impact simulation, the PM scheme can effectively describe the fracturing process, while the MPM scheme can handle the impact problem without the need for master/slave nodal treatment at the contact surface.

4. During the fracturing process, the bar target starts to break when the generated tensile wave becomes large enough, and the broken region would initiate at the given position. Thus, the proposed procedure has the potential of effectively dealing with the tensile spalling.

The future efforts are required to develop the proposed procedure for general applications, and to perform verification and validation for three-dimensional cases.

Compliance with ethical standards

Conflict of interest On behalf of all authors, the corresponding author states that there is no conflict of interest.

References

1. Jirasek M (1998) Nonlocal models for damage and fracture: comparison of approaches. Int J Solids Struct 35(31–32):4133–4145
2. Lu P, Lee HP, Lu C, Zhang PQ (2006) Dynamic properties of flexural beams using a nonlocal elasticity model. J Appl Phys 99(7):073510
3. Oliver J (1996) Modelling strong discontinuities in solid mechanics via strain softening constitutive equations. Part 1: fundamentals. Int J Numer Methods Eng 39(21):3575–3600
4. Oliver J, Huespe AE, Pulido MDG, Chaves E (2002) From continuum mechanics to fracture mechanics: the strong discontinuity approach. Eng Fract Mech 69(2):113–136
5. Silling SA, Askari E (2005) A meshfree method based on the peridynamic model of solid mechanics. Comput Struct 83(17–18):1526–1535
6. Warren TL, Silling SA, Askari A, Weckner O, Epton MA, Xu J (2009) A non-ordinary state-based peridynamic method to model solid material deformation and fracture. Int J Solids Struct 46(5):1186–1195
7. Lai X, Ren B, Fan H, Li S, Wu CT, Regueiro RA, Liu L (2015) Peridynamics simulations of geomaterial fragmentation by impulse loads. Int J Numer Anal Methods Geomech 39(12):1304–1330
8. Sarego G, Le QV, Bobaru F, Zaccariotto M, Galvanetto U (2016) Linearized state-based peridynamics for 2-D problems. Int J Numer Methods Eng 108(10):1174–1197
9. Silling SA (2017) Stability of peridynamic correspondence material models and their particle discretizations. Comput Methods Appl Mech Eng 322:42–57
10. Nicely C, Tang S, Qian D (2018) Nonlocal matching boundary conditions for non-ordinary peridynamics with correspondence material model. Comput Methods Appl Mech Eng 338:463–490
11. Lu J, Zhang Y, Muhammad H, Chen Z, Xiao Y, Ye B (2019) 3D analysis of anchor bolt pullout in concrete materials using the non-ordinary state-based peridynamics. Eng Fract Mech 207:68–85
12. Silling SA, Epton M, Weckner O, Xu J, Askari E (2007) Peridynamic states and constitutive modeling. J Elast 88(2):151–184
13. Silling SA, Lehoucq RB (2008) Convergence of peridynamics to classical elasticity theory. J Elast 93(1):13
14. Boresi AP, Schmidt RJ (2012) Advanced mechanics of materials. Wiley, New York
15. Chen WF, Saleeb AF (2013) Constitutive equations for engineering materials: elasticity and modeling, 37th edn. Elsevier, Amsterdam
16. Antman SS (1995) Nonlinear problems of elasticity. Springer, New York
17. Anderson TL (2017) Fracture mechanics: fundamentals and applications. CRC Press, Boca Raton
18. Hughes TJ (2012) The finite element method: linear static and dynamic finite element analysis. Courier Corporation, North Chelmsford
19. Macek RW, Silling SA (2007) Peridynamics via finite element analysis. Finite Elem Anal Des 43(15):1169–1178
20. Areias P, Msekh MA, Rabczuk T (2016) Damage and fracture algorithm using the screened Poisson equation and local remeshing. Eng Fract Mech 158:116–143
21. Areias P, Rabczuk T, Camanho PP (2014) Finite strain fracture of 2D problems with injected anisotropic softening elements. Theor Appl Fract Mech 72:50–63
22. Areias P, Dias-da-Costa D, Sargado JM, Rabczuk T (2013) Element-wise algorithm for modeling ductile fracture with the Rousselier yield function. Comput Mech 52(6):1429–1443
23. Zhang X, Chen Z, Liu Y (2016) The material point method: a continuum-based particle method for extreme loading cases. Academic Press, Cambridge
24. Sulsky D, Chen Z, Schreyer HL (1994) A particle method for history-dependent materials. Comput Methods Appl Mech Eng 118(1–2):179–196
25. Bardenhagen SG, Kober EM (2004) The generalized interpolation material point method. Comput Model Eng Sci 5(6):477–496
26. Sadeghirad A, Brannon RM, Burghardt J (2011) A convected particle domain interpolation technique to extend applicability of the material point method for problems involving massive deformations. Int J Numer Methods Eng 86(12):1435–1456
27. Parks ML, Lehoucq RB, Plimpton SJ, Silling SA (2008) Implementing peridynamics within a molecular dynamics code. Comput Phys Commun 179(11):777–783
28. He X, Wang H, Wu E (2017) Projective peridynamics for modeling versatile elastoplastic materials. IEEE Trans Vis Comput Graph 24(9):2589–2599
29. Mitchell JA (2011) A nonlocal ordinary state-based plasticity model for peridynamics (No. SAND2011-4974C). Sandia National Lab.(SNL-NM), Albuquerque, NM (United States)
30. Littlewood DJ (2015) Roadmap for peridynamic software implementation. SAND Report, Sandia National Laboratories, Albuquerque, NM and Livermore, CA
31. Liu W, Hong JW (2012) Discretized peridynamics for linear elastic solids. Comput Mech 50(5):579–590
32. Bobaru F, Yang M, Alves LF, Silling SA, Askari E, Xu J (2009) Convergence, adaptive refinement, and scaling in 1D peridynamics. Int J Numer Methods Eng 77(6):852–877
33. Littlewood DJ (2010) Simulation of dynamic fracture using peridynamics, finite element modeling, and contact. In: Proceedings of the ASME 2010 international mechanical engineering congress and exposition (IMECE)
34. Jiang S, Chen Z, Sewell TD, Gan Y (2015) Multiscale simulation of the responses of discrete nanostructures to extreme loading conditions based on the material point method. Comput Methods Appl Mech Eng 297:219–238